Analysis of Solute Distribution during the Solidification of Low Alloyed Steels

Carlos Cicutti[1], Roberto Boeri[2]

[1] Center for Industrial Research, TENARIS, Campana, Argentina; [2] INTEMA, Facultad de Ingeniería, Universidad Nacional de Mar del Plata - CONICET, Mar del Plata, Argentina

A numerical model that estimates the interdendritic segregation during the solidification of multicomponent low alloyed steels is presented. Some special features related to the solidification of these steels, like peritectic reaction, dendrite arm coarsening and inclusion precipitation, are taken into account by the model. Model results were extensively compared with experimental data published in the literature. In general, a good agreement between calculated and measured results was verified. Furthermore, the model was used to investigate the effect of steel composition on cracking tendency. Results showed that an increment of phosphorus and carbon content extends the solidification time in the vulnerable period, which may increase the risk of internal defects. Additionally, a peak contraction is observed for steels with carbon content around 0.10 %, which is in agreement with the lower mould heat transfer and higher surface defect index observed for these steels in plant data.

Keywords: microsegregation, solidification, mathematical modeling, low alloyed steels, cracking tendency, continuous casting

Introduction

Solute elements normally segregate in the interdendritic liquid during alloy solidification, promoting local variations in the material composition. This short-range composition change (usually known as 'microsegregation') modifies the temperature range where solidification occurs and can affect the quality of cast products. Furthermore, the segregation pattern originating during solidification may not be completely eliminated in subsequent operations, affecting the properties of the final product.

Mathematical models of different degrees of complexity and sophistication have been developed in the last years to evaluate the microsegregation of alloys [1]. Some of these models have been used to analyse the solidification of multicomponent steels, including specific features in their formulation, like the evolution of peritectic reaction [2-10], the coarsening of dendritic arms [5,7,10], the precipitation of manganese sulphides inclusions in the interdendritic liquid [3-5,7-9,11], the solute homogenization [3] and the thermal contraction after solidification [9,12]. In the present work, a mathematical model was developed to predict solute redistribution during the solidification and subsequent cooling of low alloyed steels that includes all the above mentioned features. Model results were compared with abundant experimental data published in the literature. Additionally, calculations were performed to investigate the effect of steel composition on the cracking tendency during solidification.

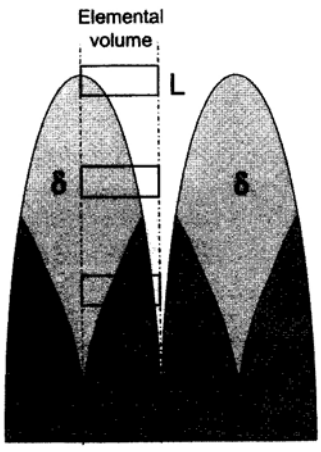

Figure 1. Definition of elemental volume between dendrite arms.

Model Development

When steels are solidified under regular industrial conditions, fully dendritic structures are normally developed. Under this condition, the microsegregation patterns developed during solidification can be assessed by describing the change in composition along a line crossing secondary dendrite arms. The model developed in this study calculates the evolution of the chemical composition within an elemental volume located between two neighbouring secondary dendrite arms, as originally proposed by Brody and Flemings [13], see **Figure 1**. As the solidification progresses, the solid-liquid interface moves from the side of the elemental volume laying at the dendrite axis, to the opposite. This model was initially used by Schwerdtfeger [11] to evaluate the microsegregation during steel solidification. Thereafter, the model has been extensively used by other researchers. As shown below, in the present case the model has been slightly modified to incorporate the dendrite arm coarsening, as suggested by Kirkwood [14-15].

The following assumptions are made in the model: (a) dendrite arms are platelike and symmetrical, (b) liquid is fully mixed at all times, (c) both the solid-liquid and the austenite-ferrite interfaces are at thermodynamic equilibrium, (d) liquid and solid density are equal and macrosegregation effects are ignored, (e) liquid undercooling is neglected, (f) the solid-liquid interface moves with a given law and the time required to complete the solidification (local solidification time) is known.

As complete mixing is assumed in the interdendritic liquid, there are no solute gradients in the liquid phase. On the other hand, solute distribution in the solid phase is controlled by diffusion. Therefore, the change in concentration (C) as a function of time (t) and distance from the dendrite arm axis (x) can be calculated by solving the second Fick's equation.

$$\frac{\partial}{\partial x}\left(D_i^p \frac{\partial C_i^S}{\partial x}\right) = \frac{\partial C_i^S}{\partial t} \tag{1}$$

Equation (1) has to be solved for each component in a domain with moving boundaries. As shown in pioneer papers [2,16], numerical methods are useful for the resolution of this type of problems. In the present work, an implicit finite difference scheme [17] was used to solve the former equation for each component. The elemental volume shown in Figure 1 is divided into a fixed number of nodes along the x axis. In each step, the position of the solid-liquid interface is moving one node forward. The time interval is updated in each step in order to fit with the prescribed growth law.

In the former equation, C_i^S is the concentration of solute i in the solid phase, and D_i^p is the diffusion coefficient of i in the phase p of iron. In low alloyed steels, p can be austenite (γ) or ferrite (δ). The dependence of the diffusion coefficient with temperature can be expressed as follows:

$$D_i^p = D_{O_i}^p \cdot \exp(-Q_i^p / RT) \tag{2}$$

Data of the pre-exponential term (D_O^P) and the activation energy (Q^P) for different solutes (C, Mn, Si, P, S, Cr, Mo and Ni) in ferrite and austenite were collected from several sources [3,6,10,18-21]. The values used in the calculations are listed in **Table 1**.

Due to the symmetry assumed in the dendrites morphology, the concentration gradient at the dendrite axis is zero, therefore the following boundary condition can be defined for every component:

$$\left(\partial C_i^S / \partial x\right)_{x=0} = 0 \tag{3}$$

Taking into account that dendrite arms coarsen during solidification [22], mass balances at the moving solid-liquid interface lead to the second set of boundary conditions [14-15]:

$$\begin{aligned} C_i^L \left(1 - k_i^p\right) dx &= D_i^p \left(\partial C_i^S / \partial x\right)_{x=X} dt \\ &+ (\lambda - X)\, dC_i^L + \left(C_i^L - C_i^O\right) d\lambda \end{aligned} \tag{4}$$

Where C_i^O and C_i^L are the initial and liquid concentration of component i, X is the position of the solid-liquid interface, λ is the instantaneous dendrite arm spacing and k_i^p is the solid-liquid partition coefficient, see Table 1.

Different investigations [22-23] have shown that the rate of secondary dendrite arm coarsening is a function of the time elapsed in the solid-liquid region. Fitting the results of experimental data published in the literature [24] for steels solidified at different cooling rates, the following expression was obtained:

$$\lambda = 26.1 \cdot t^{0.38} \tag{5}$$

In general, linear or parabolic growth laws have been proposed in microsegregation models [5,8,13,25]. In this case, a more general dependency has been considered:

$$\left(X/\lambda^F\right) = \left(t/t_S\right)^n \tag{6}$$

Table 1. Distribution and diffusion coefficients of solute elements [3,6,10,18-21].

Element	$k^{\delta/L}$	D_O^{δ} 10^{-4} (m^2/s)	Q^{δ} 10^5 (J/mol)	$k^{\gamma/L}$	D_O^{γ} 10^{-4} (m^2/s)	Q^{γ} 10^5 (J/mol)
C	0.196	0.0127	0.811	0.353	0.150	1.428
Mn	0.760	0.76	2.253	0.780	0.055	2.503
Si	0.77	8.00	2.500	0.520	0.300	2.524
P	0.23	2.90	2.310	0.130	0.010	1.835
S	0.050	4.56	2.155	0.035	2.400	2.243
Cr	0.91	2.40	2.398	0.76	0.001	2.190
Mo	0.74	3.47	2.414	0.60	0.068	2.469
Ni	0.79	1.60	2.400	0.90	0.340	2.824

Where λ^F is the final dendrite arm spacing and t_S is the local solidification time. Combining equations (5) and (6), the evolution of the solid fraction (f_s) with the time can be calculated as follows:

$$f_S = \left(X/\lambda\right) = \left(t/t_S\right)^{n-0.38} \tag{7}$$

For all the calculations shown below, a linear variation of the solid-liquid interface position was adopted (n=1). In this way, the solid fraction grows with an exponent of 0.62, which is intermediate between the linear and parabolic laws.

In some applications, the average cooling rate (instead of t_S) can be specified. In such cases, the developed program iteratively changes t_S until the calculated average cooling rate (T_{AV}) approaches the proposed value.

$$\dot{T}_{AV} = \frac{T_{Liq} - T_{Sol}}{t_S} \tag{8}$$

Where T_{Liq} and T_{Sol} are the liquidus and solidus temperatures calculated by the model.

As solidification progresses, the equilibrium temperature changes and, consequently, the diffusion coefficients have to be updated. In the case of binary systems, the equilibrium temperature at the solid-liquid interface can be evaluated directly from phase diagrams. However, for multicomponent systems, computation of this temperature is more complex. Different approaches have been adopted in the literature to estimate the solid-liquid equilibrium temperature. The simplest and most often used method [3,5,8-9] calculates the contribution of each solute component assuming a linear relationship between the solute concentration in the liquid phase and the temperature drop. In other cases, a more fundamental approach has been used [4,6,12]. As the present model aims to evaluate the segregation in low alloyed steels, the multicomponent Roultian solution approximation proposed by Kobayashi et al. [6] was adopted to calculate the equilibrium temperature at the solid-liquid interface:

$$\frac{1}{T} = \frac{1}{T_{pL}} + \frac{R}{\Delta H_{pL}} \sum_{i=1}^{n} \left(1 - k_i^p\right) C_i^L \tag{9}$$

Where T_{pL} is a reference temperature, ΔH_{pL} is the latent heat of transformation and R the universal constant of gases.

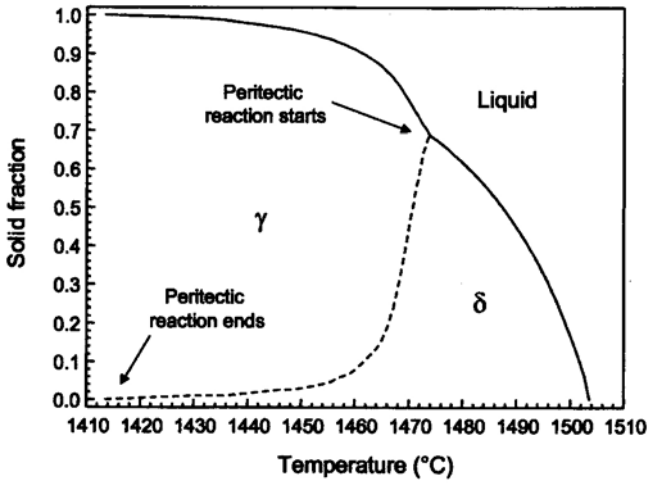

Figure 2. Calculated solid fraction (δ and γ phases) as a function of temperature for the steel composition and cooling rate shown in Table 2.

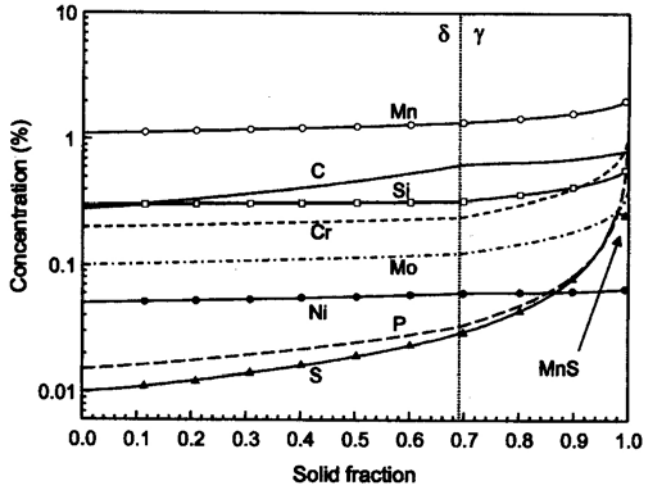

Figure 3. Evolution of solute segregation in liquid phase as solidification progresses for the steel composition and cooling rate shown in Table 2.

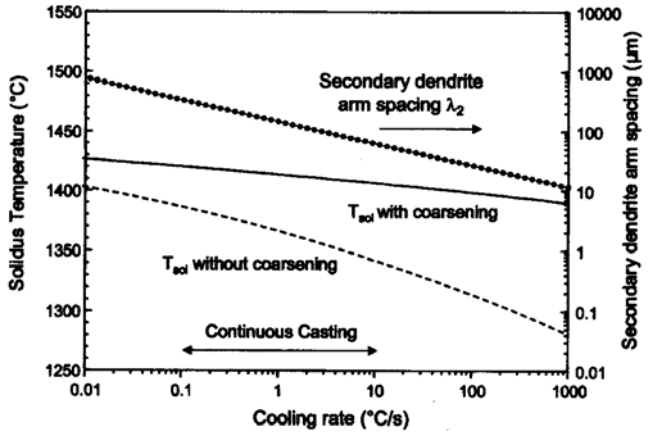

Figure 4. Effect of cooling rate on secondary dendrite arm spacing and solidus temperature with and without dendrite arm coarsening for the steel composition shown in Table 2.

In low and medium carbon steels, solidification can start in ferrite (δ) and finish in austenite (γ). Therefore, a peritectic transformation takes place during solidification. As the thermodynamic properties of solid phase (like diffusion and partition coefficients) are different for both crystalline structures, the model has to incorporate this reaction. The temperature at which the transformation starts was also calculated using the approach suggested by Kobayashi et al. [6], by an equation similar to (9). The position of the γ/δ interface is tracked using a similar procedure to that developed by Ueshima et al [3]. In this way, the proportion of each phase can be computed during the solidification process.

Segregation in the liquid phase can be affected by the precipitation of non-metallic inclusions during solidification. In low alloyed steels the most common case is the precipitation of manganese sulphides in the interdendritic liquid. The model developed takes into account this effect by assuming that MnS precipitation starts when the concentrations of manganese and sulphur at the liquid phase exceed the solubility product [11], and liquid composition is then recalculated.

Finally, in those cases where the cooling rate after solidification is known, the model can calculate solute redistribution in the solid state. In this way, the evolution of peritectic reaction and solute redistribution after solidification can be computed. As it is shown later, this is useful to estimate the effect of steel composition on thermal contraction.

Further details of the model have been reported elsewhere [26]. Numerical results were compared with available analytical solutions and an excellent agreement was found [26].

Typical Results of the Model

Once the previous equations are solved, the model can predict solute distributions in the solid and liquid phase during solidification. The evolution of temperature and the proportion of δ and γ phases can also be computed. These results can be coupled with heat transfer calculations to predict the evolution of latent heat in the solidification range. As an example, **Figure 2** shows the relationship between temperature and solid fraction for the steel composition indicated in **Table 2**. In this medium carbon steel solidification starts in δ phase but when solid fraction is around 0.70, the peritectic transformation begins. From this point, three phases are in equilibrium: liquid, ferrite and austenite. As solidification advances, the proportion of austenite is increased until the reaction is completed close to the solidification end.

Figure 3 shows the evolution of solute concentration in liquid phase as solidification progresses. Some elements (like C, Cr, Si, P and S) exhibit a noticeable change in the segregation pattern when peritectic transformation starts (f_s = 0.70) because diffusion and partition coefficients are different in γ phase (see Table 1). In particular, segregation of residual elements (P and S) is drastically increased in the last stages of solidification. Near the end of solidification, manganese sulphides begin to precipitate in the liquid phase, so a decrease in sulphur segregation is observed. This precipitation can partially hinder the effect of sulphur in extending the solidification range.

Figure 4 shows the influence of the cooling rate on the solidus temperature of the alloy and the secondary dendrite arm spacing, see equation (5). Calculations with and without dendrite arm coarsening during solidification were performed. As the cooling rate is increased, a higher interdendritic segregation is obtained (due to the shorter time available for back diffusion of solutes) promoting a reduction of the solidus temperature. However, when coarsening of dendrite arms is taken into account, the reduction of the solidus temperature becomes less important. In particular, the decrease of the solidus temperature within the cooling rate range typically found in the continuous casting process (0.1-10 °C/s), is relatively small (about 15 °C for tested conditions).

Once solidification is finished, diffusion of solute elements in solid state can reduce the concentration gradients. Calculations were performed to evaluate the effect of different cooling rates after solidification on the degree of homogenization (in this case defined as the ratio between the maximum and minimum concentration of the solutes found along the half-dendrite). **Figure 5** shows the results obtained for carbon and manganese when three different cooling rates were considered: 0.1, 1.0 and 10 °C/s. Carbon gradients are quickly eliminated due to its high diffusion coefficient (see Table 1). On the other hand, a high degree of manganese segregation remains after cooling, even for the lowest cooling rate evaluated. It has been shown [27-28] that this local variation in manganese content locally modifies the temperature at which γ-α transformation starts (A_{r3} temperature) promoting the development of banded structures in rolled products.

Comparison with Experimental Data

Liquidus and solidus temperature. In order to compare the results of the model with experimental values, data measured by different authors were collected [6,24,29-31]. Only those studies reporting results on low alloyed steels were taken into account. A total of 90 cases of liquidus determinations and 64 of solidus measurements were selected, which correspond to a wide range of steel compositions, listed in **Table 3**.

Calculated and measured values are compared in **Figure 6**. In general, a good agreement between both magnitudes is verified. A slightly larger scatter is observed for solidus temperatures, which can be partially attributed to the experimental difficulties to obtain accurate determinations. Statistical results are summarized in **Table 4**. The average differences between calculated and measured values are close to zero for both temperatures, indicating a good performance of the model.

Zero ductility and zero strength temperature. Different investigations have suggested that the mechanical properties of steels at high temperatures are closely connected with the solidification process [8,32-33]. When solidification starts, the liquid fraction is high and no mechanical strength is observed. However, as the temperature decreas-

Table 2. Steel composition and cooling rate used in model calculations.

Steel composition (wt.%)								Cooling rate
C	Mn	Si	P	S	Cr	Mo	Ni	CR (°C/s)
0.28	1.10	0.20	0.015	0.010	0.30	0.10	0.05	1.0

Table 3. Range of steel composition corresponding to the selected experimental data [6,24,29-31].

	Steel composition (wt.%)								CR
	C	Mn	Si	P	S	Cr	Mo	Ni	(°C/s)
Min	0.04	0.02	0.01	0.003	0.001	0.00	0.00	0.00	0.10
Max	1.01	2.00	2.07	0.040	0.025	5.20	0.99	3.69	2.00

Table 4. Comparison between measured and calculated values.

	ΔT (measured – calculated)	
	Liquidus	Solidus
Mean (°C)	-1.81	0.53
Std deviation (°C)	3.73	17.34
Number of data	94	56

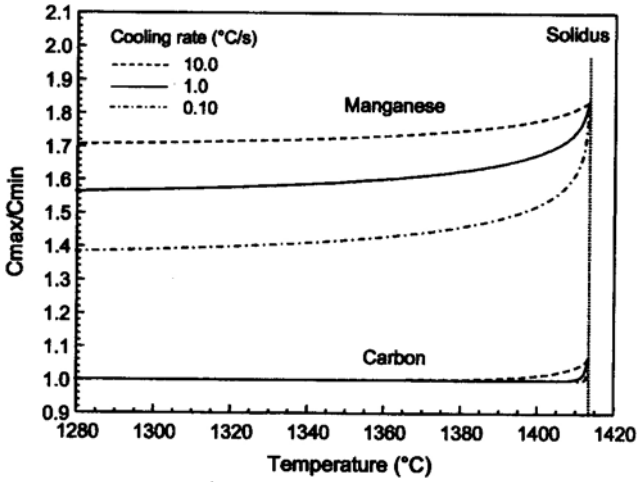

Figure 5. Effect of cooling rate after solidification on the degree of segregation of carbon and manganese. Base steel composition and cooling rate during solidification are shown in Table 2.

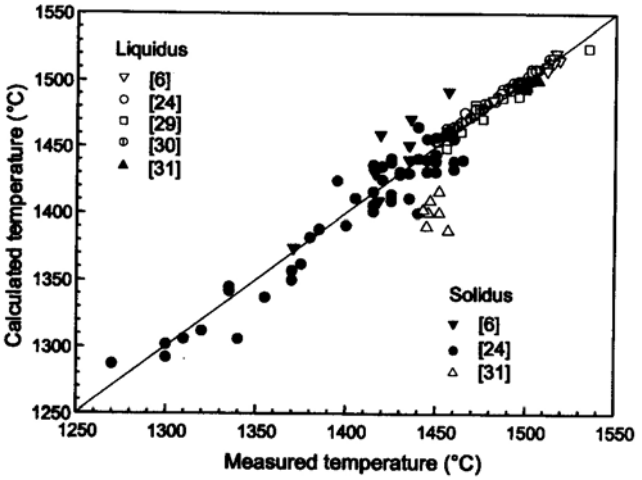

Figure 6. Comparison between measured [6,24,29-31] and calculated liquidus and solidus temperatures.

es, the solid fraction increases and dendrites start to contact each other. When this dendrite bridging is strong enough, mechanical forces can be transmitted during tensile tests and a strength different from zero can be measured. However, as liquid films remain between dendrite arms, the fracture is mostly brittle and the reduction of area of the sample is close to zero. The minimum temperature that exhibits nil strength is usually known as the Zero Strength Temperature (ZST). Although there are some discrepancies on the exact solid fraction at which the ZST is obtained, a value around 0.7-0.8 is normally accepted [8,32-33]. For lower temperatures, the amount of interdendritic liquid films is reduced and a ductile fracture can be obtained. The minimum temperature at which a nil reduction of area is observed during hot tensile tests is normally called the Zero Ductility Temperature (ZDT). In general, it is agreed that this temperature is close to the non-equilibrium solidus temperature.

Table 5. Range of steel composition corresponding to the selected experimental data [33-40].

	Steel composition (%)				
	C	Mn	Si	P	S
Min	0.015	0.01	0.005	0.001	0.001
Max	1.60	2.38	0.42	0.036	0.280

Table 6. Base steel composition used in calculations (wt.%).

C	Mn	Si	P	S
0 – 0.80	1.50	0.20	0.015	0.010

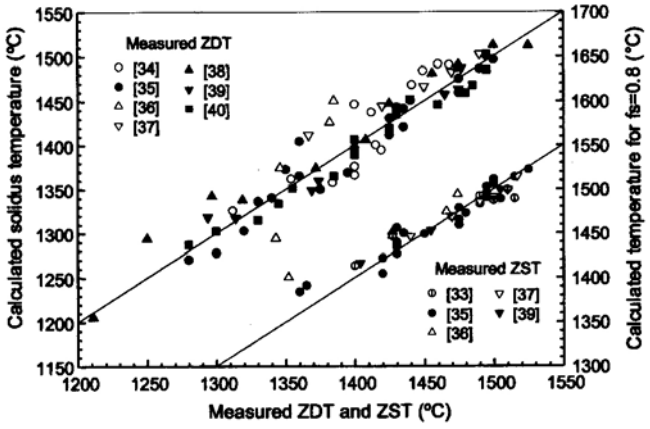

Figure 7. Comparison between Zero Ductility Temperature (ZDT) and Zero Strength Temperature (ZST) measured by different authors [33-40] and calculated by the present model.

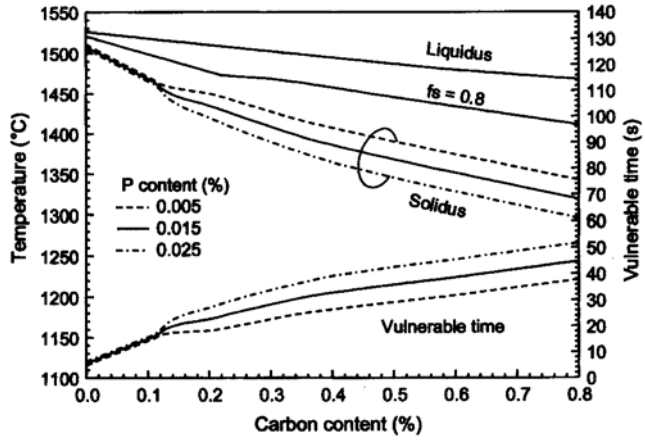

Figure 8. Influence of carbon and phosphorus content on the vulnerable time and some relevant temperatures (liquidus, solidus and fs = 0.8) for a steel with the base composition shown in Table 6.

Data of mechanical properties measured at high temperatures by different authors [33-40] were collected and compared with model calculations. For calculations, chemical composition and cooling rates reported in the tests were used as input data for the model. The range of steel composition investigated in these studies is listed in **Table 5**.

Figure 7 compares the solidus temperature estimated by the model with the ZDT measured by different authors. For most of the cases a good agreement between both magnitudes is observed. Similarly, the calculated temperature for a solid fraction of 0.8 is compared with ZST measurements. Although a larger dispersion is observed in the results, still a reasonable agreement between calculated and measured temperatures is verified.

Influence on the Steel Crack Sensitivity

Effect of steel composition on internal cracking. Most of the internal cracks observed in the continuous casting products are originate during the solidification process [41]. Metallographic analyses of these cracks usually exhibit an interdendritic propagation with a smooth appearance of the fracture surface, suggesting that cracks are opened by a hot tearing mechanism [41]. As discussed in the previous section, the most vulnerable period is between the ZDT and ZST. Therefore, a reasonable way to compute the cracking tendency of steels is by calculating the time interval from $f_s = 0.8$ to $f_s = 1.0$, which is in agreement with the procedure previously proposed in the literature [42]. A longer time in the vulnerable region increases the probability that an external stress or strain that exceeds the critical value is applied. There are several sources of thermal and mechanical stresses in the continuous casting process. Particularly, roll bending, roll misalignment and strand bulging may introduce severe tensile stresses in the solidification front [41]. Similarly, sudden changes in the spray cooling pattern can also induce thermal stresses in the solid-liquid region.

In order to investigate the influence of steel composition on the internal cracking tendency, calculations were performed using the microsegregation model. The effect of changing carbon and phosphorus content on a steel with the composition shown in **Table 6** was analysed. Results are summarized in **Figure 8**. In addition to liquidus and solidus temperature, the temperature that corresponds to a solid fraction of 0.8 (ZST) and the vulnerable time are also plotted. As the carbon content increases, the solidification interval and the vulnerable period increase. Besides, an increment of the phosphorus content reduces the solidus temper-

ature without changing ZST, so longer vulnerable times are obtained. This effect is more noticeable for steel carbon contents above 0.12 %, where a part of the solidification proceeds in the γ phase. These results are in good agreement with plant observations, which indicate that these elements (carbon and phosphorus) are detrimental to steel internal quality [42-44].

Surface cracking in peritectic steels. It is widely accepted that steels with a carbon content close to 0.10 % exhibit a distinct behaviour during casting. These steels (usually named as 'peritectic') exhibit a lower heat transfer in the continuous casting mould [45-49] and are more prone to surface cracking problems [50-54]. Both effects have been related to the larger shrinkage produced during the phase change involved in the peritectic reaction [47-48]. The model developed in previous sections was used to investigate the contraction behaviour of these steels.

As the steel is cooled down from a reference temperature T_{Ref} to a temperature T, the thermal contraction (ε^{th}) can be estimated from the following expression [55]:

$$\varepsilon^{th}(T) = \sqrt[3]{\frac{\rho(T_{Ref})}{\rho(T)}} - 1 \qquad (10)$$

Where ρ is the density of steel. When only the contraction in the solid state is computed, the reference value is normally the solidus temperature [55]. Some authors [9,12] assume that the dendritic structure becomes packed enough to allow the material to behave like a solid at temperatures slightly above solidus, and adopt the temperature that corresponds to a solid fraction of 0.8-0.9 as reference for calculations. As there is not complete agreement on this topic, in the present work solidus temperature was chosen as reference value for contraction calculations.

If several phases (liquid, ferrite and austenite) are present at a given temperature, the density of the mixture can be calculated by using the following expression [56]:

$$\rho(T) = \frac{1}{\sum_{n=1}^{p} \left(f_n(T) / \rho_n(T) \right)} \qquad (11)$$

Where f_n and ρ_n are the mass fraction and density of each one of the phases present at temperature T. The densities of the different phases are not only a function of temperature but also depend on the steel composition [55-57]. In this case, the formulas derived by Miettinen and Lohuenkilpi [56] were used to compute the density of liquid steel, ferrite and austenite. From model calculations, the fraction of each phase and their mean composition can be evaluated as a function of temperature. Hence, density and then thermal contraction can be computed using equation (10).

Calculations were carried out to investigate the effect of steel carbon content on the thermal contraction. The base steel composition used in the calculations is shown in **Table 6**. Carbon content was varied from 0 to 0.40 % and a cooling rate of 10 °C/s was adopted. Thermal contraction calculations were carried out for different temperature intervals below solidus (ΔT = 20, 40, 60, 80 and 100 °C). Results are summarized in **Figure 9**. Although the position of the contraction peak is slightly modified with the temperature range considered, it is clear that a maximum shrinkage is obtained for steel carbon contents in the range 0.09-0.12 %. Similar results have also been reported by other researchers [9,12,55].

In **Figure 10**, results of thermal contraction are compared with mould heat flux data measured by different authors [45-48]. In order to make comparable the data from different sources, mould heat flux has been referred to that observed for low or high carbon contents. In this way a 'Relative heat flux' has been obtained and plotted against steel carbon content. Despite the different continuous casting machines considered (slabs, blooms and billets) and the differences in the base steel composition, the computed thermal contraction results follow the same trend of measured values.

Finally, reported plant data [50-54] of defect ratio for different steel carbon contents were collected. For the purpose of comparison, the values reported by different steel plants were normalized adopting a defect index that ranges from 0 to 1 (1 corresponding to the maximum defect ratio reported in each specific plant). Compiled results are shown in

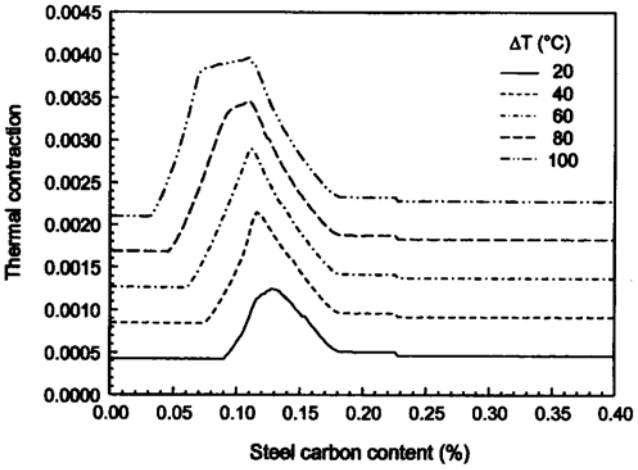

Figure 9. Effect of steel carbon content on thermal contraction during solidification.

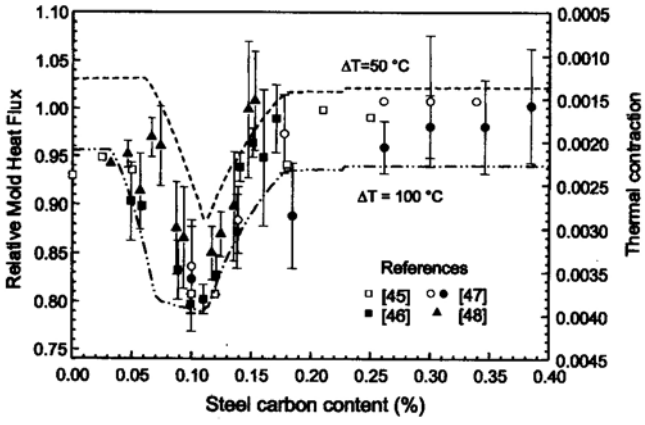

Figure 10. Effect of steel carbon content on the mould heat transfer measured in different plants [45-48]. Comparison with thermal contraction calculations.

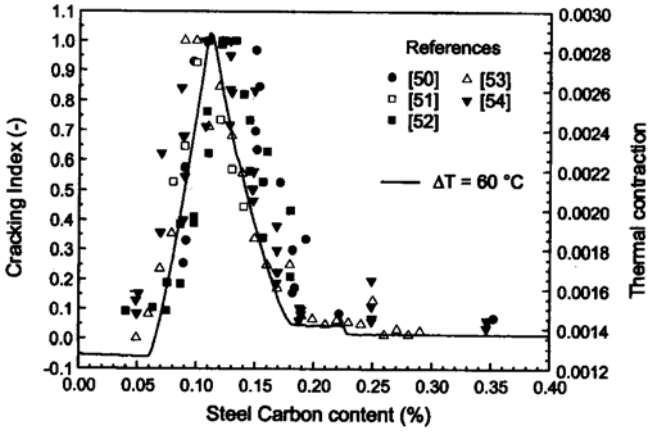

Figure 11. Influence of steel carbon content on the cracking index in different steel plants [50-54]. Comparison with thermal contraction calculations.

Figure 11. Again, the maximum defect index is in good agreement with the position of the peak contraction calculated by the model.

Conclusions

A model that estimates the segregation of solutes during the solidification of low alloyed steels was developed. Some specific features that are relevant to the solidification of these steels, like the peritectic reaction, the dendrite arm coarsening, the precipitation of inclusions and the solute homogenization in the solid after the solidification is complete, were included in the model. Calculations showed that all these features can significantly affect the solute redistribution during and after solidification. For example, peritectic transformation increases the segregation of some solutes in the interdendritic liquid but dendrite arm coarsening can attenuate this effect. While for elements of high diffusion coefficients (as carbon) concentration gradients become rapidly homogenized after solidification, for slow diffusing species (like manganese) the solute distribution is affected by the cooling rate imposed after solidification.

Model results were extensively compared with experimental data published in the literature. In most cases a good agreement between calculated and measured values was verified. Particularly, the model proved to be effective in predicting ZDT and ZST for a large range of steel compositions. As the material is more susceptible to fail in the temperature range between ZDT and ZST, the time elapsed in this range during solidification might be related to the internal cracking tendency. Calculations showed that this time interval increases as the content of residual elements, like phosphorus, raises. This effect is even more significant for higher carbon contents, when solidification proceeds in austenitic phase. A similar trend in the cracking tendency of continuously cast products is usually reported in the literature.

Finally, the model was also used to evaluate the effect of steel chemistry on thermal contraction during cooling. Calculated results show a peak contraction around 0.10 % C, which is in agreement with both the lower mould heat transfer and the higher surface defect index observed for these steels in industrial practice.

(A2005112; received on 7 April 2005, in final form on 3 June 2005)

Contact: Dr. Carlos Cicutti
Center for Industrial Research TENARIS
Dr. Simini 250
2804 Campana / Argentina

References

[1] T. Battle: Int. Materials Review, 37 (1992), N° 6, 249-270.
[2] Y. Chuang, D. Reinisch, K. Schwerdtfeger: Metallurgical Transactions A, 6A (1975), 235-238.
[3] Y. Ueshima, S. Mizoguchi, T. Matsumiya, H. Kajioka: Metallurgical Transactions B, 17B (1986), 845-859.
[4] J. Miettinen: Metallurgical Transactions A, 23 A (1992), N° 4, 1155-1170.
[5] Y. Won, B. Thomas: Metallurgical and Materials Transactions A, 32 A (2001), 1755-1767.
[6] S. Kobayashi, T. Nagamichi, K. Gunji: Transactions ISIJ, 28 (1988), 543-552.
[7] A. Howe: Applied Scientific Research, 44 (1987), 51-59.
[8] M. Cornelissen: Ironmaking and Steelmaking, 13 (1986), N° 4, 204-212.
[9] K. Kim, T. Yeo, K. Oh, D. Lee: ISIJ Int., 36 (1996), N° 3, 284-289.
[10] A. Howe, D. Kirkwood: Materials Science and Technology, 16 (2000), 961-967.
[11] K. Schwerdtfeger: Archiv Eisenhüttenwesen, 41 (1970), 923-937.
[12] J. Miettinen: Scandinavian Journal of Metallurgy, 22 (1993), 317-324.
[13] H. Brody, M. Flemings: Transactions TMS-AIME, 236 (1966), 615-624.
[14] D. Kirkwood: Materials Science and Engineering, 65 (1984), 101-109.
[15] A. Ogilvy, D. Kirkwood: Applied Scientific Research, 44 (1987), 43-49.
[16] Y. Chuang, W. Wepner, K. Schwerdtfeger: Archiv Eisenhüttenwesen, 44 (1973), 243-250.
[17] J. Crank: The Mathematics of Diffusion, Clarendon Press, 1975.
[18] J. Miettinen: Metallurgical and Materials Transactions B, 28 B (1997), 281-297.
[19] A. Kagawa, T. Okamoto: Material Science and Technology, (1986), 997-1008.
[20] Z. Morita, T. Tanaka: ISS Process Technology Conference, 1986, p.781-789.
[21] M Schneider, C Beckermann: Metallurgical and Materials Transactions A, 26 A, (1995), 2373-2388.
[22] T. Kattamis, J. Coughlin, M. Flemings: Transactions TMS-AIME, 239 (1967), 1504-1511.
[23] W. Kurz, D. Fisher: Fundamentals of solidification, Trans Tech Publications, 3rd Edition, 1992.
[24] A guide to the solidification of steels, Jernkontoret, Stockholm, 1977.
[25] S. Kobayashi: Transactions ISIJ, 28 (1988), 535-542.
[26] C. Cicutti, R. Boeri: 13th IAS Steelmaking Seminar, 2001, 711-718.
[27] R. Grossterlinden, R. Kawalla, U. Lotter, H. Pircher: Steel Research, 63 (1992), N° 8., 331-336.
[28] G. Krauss: Metallurgical and Materials Transactions B, 34B (2003), 781-792.
[29] O. Hammar, G. Grünbaum: Scandinavian Journal of Metallurgy, 3 (1974), 11-20.
[30] A. Howe: Ironmaking and Steelmaking, 15 (1988), N° 3, 134-142.
[31] L. Ericson: Scandinavian Journal of Metallurgy, 6 (1977), 116-124.
[32] A. Yamanaka, K. Nakajima, K. Yasumoto, H. Kawashima, K. Nakai: Revue de Metallurgie, (1992), N° 7-8, 627-633.
[33] T. Nakagawa, T. Umeda, J. Murata, Y. Kamimura, N. Niwa: ISIJ Int., 35 (1995), N° 6, 723-729.
[34] F. Weinberg: Metallurgical Transactions B, 10B (1979), 219-227.
[35] E. Schmidtmann, F. Rakoski: Archiv Eisenhüttenwesen, 54 (1983), N° 9, 357-362.

[36] C. Adams: Open Hearth Conference, 1971, Vol. 54, p.290-302.
[37] G. Shin, T. Kajitani, T. Suzuki, T. Umeda: Tetsu to Hagané, 78 (1992), 587-593.
[38] H. Suzuki, S. Nishimura, Y. Nakamura: Transactions ISIJ, 24 (1984), 54-59.
[39] D. Seol, Y. Won, K. Oh, Y. Shin, C Yim: ISIJ Int., 40 (2000), N° 4, 356-363.
[40] W. Bleck, W. Dahl, G. Picht, G. Pariser: Steel Research, 72 (2001), N° 11-12, 496-502.
[41] K. Sorimachi, J. Brimacombe: Metallurgical Transactions B, 8B (1977), 489-505.
[42] T. Clyne, M. Wolf, W. Kurz: Metallurgical Transactions B, 13 B (1982), 259-266.
[43] M. Wolf: 1st European Conference on Continuous Casting, 1991, Vol.2, p.2.490-2.499.
[44] R. Jauch: Stahl und Eisen, 98 (1978), N° 6, 244-254.
[45] S. Singh, K. Blazek: Journal of Metals, (1974), N° 10, 17-27.
[46] M. Mundim, J. Pimenta, C. Valadares, P. Pereira: Continuous Casting, 1985, p.50.1-50.6.
[47] A. Grill, J. Brimacombe: Ironmaking and Steelmaking, (1976), N° 2, p.76-79.
[48] C. Cicutti, M. Valdez, T. Pérez, G. Di Gresia, W. Balante, J. Petroni: 85th ISS Steelmaking Conference, Nashville, 2002, p. 97-107.
[49] M. Wolf: Transactions ISIJ, 20 (1980), 710-717.
[50] W. Irving, A. Perkins, R. Gray: Ironmaking and Steelmaking, 11 (1984), N° 3, 146-151.
[51] H. Tsai, J. Mastervich: ISS Steelmaking Conference, 1988, Vol. 71, p.167-173.
[52] T. Kappey: ISS Steelmaking Conference, 1992, Vol. 75, p.543-547.
[53] K. Blazek: Iron and Steelmaker, (1988), N° 6, 38-39.
[54] R. Gray, A. Perkins, B. Walker: TMS Solidification and casting of metals, 1979, p.300-306.
[55] A. Jablonka, K. Harste, K. Schwerdtfeger: Steel Research, 62 (1991), N° 1, 24-33.
[56] J. Miettinen, S. Louhenkilpi: Metallurgical and Materials Transactions B, 25 B (1994), 909-916.
[57] I. Jimbo, A. Cramb: Metallurgical Transactions B, 24 B (1993), 5-10.